



Convective Characteristics of the Madden–Julian Oscillation over the Central Indian Ocean Observed by Shipborne Radar during DYNAMO

WEIXIN XU AND STEVEN A. RUTLEDGE

Colorado State University, Fort Collins, Colorado

(Manuscript received 22 November 2013, in final form 17 February 2014)

ABSTRACT

This study investigates the convective population and environmental conditions during three MJO events over the central Indian Ocean in late 2011 using measurements collected from the Research Vessel (R/V) *Roger Revelle* deployed in Dynamics of the MJO (DYNAMO). Radar-based rainfall estimates from the *Revelle* C-band radar are first placed in the context of larger-scale Tropical Rainfall Measuring Mission (TRMM) rainfall data to demonstrate that the reduced *Revelle* radar range captured the MJO convective evolution. Time series analysis and MJO phase-based composites of *Revelle* measurements both support the “recharge–discharge” MJO theory. Time series of echo-top heights indicate that convective deepening during the MJO onset occurs over a 12–16-day period. Composite statistics show evident recharging–discharging features in convection and the environment. Population of shallow/isolated convective cells, SST, CAPE, and the lower-tropospheric moisture increase (recharge) substantially approximately two to three phases prior to the MJO onset. Deep and intense convection and lightning peak in phase 1 when the sea surface temperature and CAPE are near maximum values. However, cells in this phase are not well organized and produce little stratiform rain, possibly owing to reduced shear and a relatively dry upper troposphere. The presence of deep convection leads the mid- to upper-tropospheric humidity by one to two phases, suggesting its role in moistening these levels. During the MJO onset (i.e., phase 2), the mid- to upper troposphere becomes very moist, and precipitation, radar echo-top heights, and the mesoscale extent of precipitation all increase and obtain peak values. Persistent heavy precipitation in these active periods helps reduce the SST and dry/stabilize (or discharge) the atmosphere.

1. Introduction

The Madden–Julian oscillation (MJO), first discovered by [Madden and Julian \(1971, 1972\)](#), is widely known as a remarkable coupled convective–wind tropical disturbance that usually develops in the Indian Ocean (IO) and slowly propagates eastward with an intraseasonal cycle of 30–60 days ([Weickmann et al. 1985](#); [Rui and Wang 1990](#); [Sui and Lau 1992](#); [Salby and Hendon 1994](#); [Wheeler and Hendon 2004](#); [Zhang 2005](#)). The MJO is the most dominant mode of intraseasonal variability in the tropics and plays important roles at climate and weather system scales ([Zhang 2013](#)). Despite decades of study, the MJO is not well understood and therefore MJO prediction skill is limited, especially

for initiation over the Indian Ocean ([Bechtold et al. 2008](#); [Kim et al. 2009](#); [Vitart and Molteni 2010](#)). Meanwhile, the MJO has been poorly simulated by several generations of general circulation models (GCMs) ([Lin et al. 2006](#); [Hung et al. 2013](#)). The representation of cumulus convection is believed to be the primary limiting factor in MJO simulation and prediction ([Randall et al. 2003](#); [Lin et al. 2006](#); [Zhang et al. 2006](#); [Benedict and Randall 2009](#)). To improve parameterizations of clouds and physical precipitation processes in numerical models, it is important to quantify the evolution of convective cloud populations and convective/microphysical characteristics, understand the interaction between convection and the local environment (e.g., moisture and heating), and quantify air–sea interactions. Indeed, these outstanding problems motivated the Dynamics of the MJO (DYNAMO; [Yoneyama et al. 2013](#)) field experiment over the central Indian Ocean (CIO) around 8°S–8°N, 72°–80°E during late 2011–early 2012.

Corresponding author address: Weixin Xu, Department of Atmospheric Sciences, Colorado State University, 3915 West Laporte Avenue, Fort Collins, CO 80521.
E-mail: wxinxu@atmos.colostate.edu

Early studies of the MJO cloud population and convective characteristics were mainly based on satellite infrared or outgoing longwave radiation (OLR) measurements (Lau and Chan 1985, 1986; Nakazawa 1988; Mapes and Houze 1993; Chen et al. 1996). These studies first pointed out the importance of cloud clusters at the scale of hundreds of kilometers [or mesoscale convective systems (MCSs)] in the MJO disturbance. Cloud populations, morphology, precipitation evolution, and heating profiles over the western Pacific Ocean were extensively examined using data collected during the 1992/93 Tropical Ocean and Global Atmosphere Coupled Ocean–Atmosphere Response Experiment (TOGA COARE; Godfrey et al. 1998). DeMott and Rutledge (1998a) showed that the inactive MJO periods were dominated by shallow convection, while the active period had a higher frequency of deep convection. Though the inactive phase is generally characterized by lower echo-top heights, the majority of rainfall during this time was actually due to occasional vertically “intense” convection. Johnson et al. (1999) illustrated that three cloud types—namely, shallow cumulus, congestus, and cumulonimbus—are all prominent tropical convective cloud types and that these three cloud populations vary significantly with a time scale of the 30–60-day intraseasonal oscillation (MJO scale). Using TOGA COARE sounding data and satellite infrared measurements, Kikuchi and Takayabu (2004) identified a similar trimodal cumulus cloud population and found that these clouds exhibited a stepwise development across the MJO cycle. The profile of total heating in the active MJO phase is top heavy, peaking in the upper troposphere (Lin and Johnson 1996; Yanai et al. 2000). This top-heavy heating is due to enhanced stratiform precipitation fractions during the active phase of the MJO (Lin et al. 2004).

More recent studies have investigated the MJO cloud population, precipitation structure, dynamical structure, and the interaction of convection with the large-scale environment using radiosonde or satellite sounding data (Kiladis et al. 2005; Tian et al. 2006), model reanalysis (e.g., Kiladis et al. 2005; Benedict and Randall 2007), satellite precipitation retrievals (Tian et al. 2006; Morita et al. 2006; Benedict and Randall 2007), and satellite cloud measurements (Tromeur and Rossow 2010; Lau and Wu 2010; Virts et al. 2010; Riley et al. 2011; Del Genio et al. 2012; Barnes and Houze 2013). These results showed that cloud systems across the MJO cycle basically progress from shallow cumulus, to cumulus congestus, to deep convection, and finally stratiform. Shallow convection dominates during the suppressed phase, which helps to moisten and heat the lower troposphere (Kiladis et al. 2005; Tian et al. 2006; Benedict and Randall 2007) through detrainment and latent

heating of condensation (Johnson et al. 1999; Kikuchi and Takayabu 2004). This may provide a more favorable environment for subsequent convection and thus further moistening. Eventually, the column may become sufficiently moist to support deep convection. This process is the so-called recharge process in the “discharge–recharge” MJO initiation–evolution theory (Bladé and Hartmann 1993; Hu and Randall 1994; Kemball-Cook and Weare 2001). Although the low-level moistening could also be due to large-scale horizontal advection and moisture convergence (Maloney and Hartmann 1998; Maloney 2009), the importance of cloud moistening has been noted by many authors (Stephens et al. 2004; Benedict and Randall 2007; Lau and Wu 2010; Del Genio et al. 2012). In fact, moistening and heating of the lower troposphere from shallow cumulus and congestus clouds is a key factor for successful simulations of the MJO in climate models (Zhang and Song 2009; Del Genio et al. 2012).

Detailed studies of MJO convection based on surface-based radar and sounding observations are lacking. Prior to DYNAMO, the only field experiment targeting the MJO in the IO was the 2006 Research Vessel (R/V) *Mirai* Indian Ocean cruise for the Study of the MJO Onset (MISMO; Yoneyama et al. 2008). However, MISMO was relatively limited in duration and only one fairly weak MJO event was observed. The 2011/12 DYNAMO field campaign collected an unprecedented record of detailed observations from island- and ship-based radars, rawinsonde networks, airborne radar and remote sensing instrumentation, and oceanographic instrumentation over the CIO, where the MJO convective coupling develops (Yoneyama et al. 2013). A major goal of DYNAMO was to examine MJO initiation and evolution hypotheses by unraveling the MJO’s underlying physical mechanisms. The present study is particularly aimed at examining two of the three DYNAMO hypotheses. The first DYNAMO hypothesis is that deep convection can be organized into an MJO convective envelope only when the troposphere has become sufficiently moist over a large region. The second hypothesis states that specific convective populations at different stages of the MJO are essential to MJO initiation (Yoneyama et al. 2013).

The DYNAMO field campaign successfully captured several MJO events during October 2011–March 2012 (Yoneyama et al. 2013; Gottschalck et al. 2013). Sounding-derived patterns of moistening, divergence, and vertical motion confirm the stepwise progression of convection from shallow cumulus to congestus to deep convection (Johnson and Ciesielski 2013, hereafter JC13). JC13 also found the gradual moistening of the low to midtroposphere over roughly 2 weeks prior to the

TABLE 1. Cruises, instrument operations, C-band radar sampling, and radar precipitation feature (RPF) samples of R/V *Revelle* during the 2011/12 DYNAMO field campaign phase. R/V *Revelle* was largely operating in another area during cruise 1; therefore, radar data were not included for this cruise.

	Ship cruise			
	1	2	3	4
Cruise time	30 Aug–25 Sep	30 Sep–1 Nov 2011	7 Nov–10 Dec 2011	15 Dec 2011–4 Jan 2012
Time around 0°, 80.5°E	—	2–29 Oct 2011	9 Nov–5 Dec 2011	17 Dec 2011–2 Jan 2012
Radiosondes	—	8 day ^{−1}	8 day ^{−1}	8 day ^{−1}
Radar volumes	—	Every 10 min	Every 10 min	Every 10 min
RPF samples	—	134 636	137 300	38 475

MJO onset. Based on S-band radar measurements collected from Gan Island during DYNAMO, Zuluaga and Houze (2013, hereafter ZH13) found that rainfall in active periods was intermittent and occurred in episodes lasting 2–4 days. ZH13 examined the convective population within these 2–4-day rainfall episodes and showed that shallow convective echoes (SCE)/narrow deep convective cores (DCC), wide convective cores (WCC), and broad stratiform (BSR) systems were the most frequent prior to, during, and after the maximum rainfall, respectively. Using the same dataset, Powell and Houze (2013) showed that precipitation area, radar echo-top height, and tropospheric humidity rapidly increase over approximately 3–7 days prior to the MJO onset.

The current study aims to use ship-based measurements (~700 km from Gan Island) during DYNAMO to examine the evolution of convective population and the environment across the MJO life cycle and quantify their convective properties. Though ZH13 examined the population of different convective systems over Gan Island during DYNAMO, they mainly focused on 2–4-day rainfall episodes. We aim to complement their results by providing a description of the 30–60-day variability of MJO associated precipitating clouds, including morphology (both height and size), convective intensity, rainfall contributions by different types of precipitating clouds, and lightning frequency (a marker for the presence of intense tropical convection; Williams 1989; Zipser 1994; Petersen et al. 1996). Variability of all convective quantities as a function of MJO phase are further related to changes in sea surface temperature (SST), tropospheric humidity, convective available potential energy (CAPE), and deep tropospheric wind shear.

2. Data and methodology

This study uses data collected from the R/V *Roger Revelle* deployed at the northeastern site (0°, 80.5°E) of the DYNAMO northern sounding array over the CIO (Yoneyama et al. 2013). During DYNAMO, R/V *Revelle* made four cruises to the campaign area (Table 1).

We only consider measurements taken from cruises 2–4 during which time the DYNAMO observations were extensive and major MJO events were sampled (Yoneyama et al. 2013). We did not consider times when the ship was transiting to/from port or otherwise off station (Table 1). The vacancy of the *Revelle* had little influence on our results, since (fortunately) most of the missing data periods occurred during suppressed MJO phases. Tropical Rainfall Measuring Mission (TRMM) rainfall time series over our analysis period are virtually the same when including and excluding data during the off-station periods. Specific data from R/V *Revelle* include the National Aeronautics and Space Administration (NASA) TOGA C-band Doppler radar measurements and frequent radiosonde observations. Additionally, SST data from the nearby Research Moored Array for African–Asian–Australian Monsoon Analysis and Prediction (RAMA) research buoy (0°, 80.5°E) and lightning data from the Vaisala’s global lightning detection (GLD360) network are also employed.

a. Radar

1) RADAR DATA

The NASA TOGA C-band radar (Short et al. 1997) on board the R/V *Revelle* (called the *Revelle* radar) operated around the clock when the ship was on station (Table 1). The *Revelle* radar completed a full volume scan every 10 min including twenty-two 360° plan position indicator (PPI) sweeps. Five manually selected vertical cross sections [range height indicator (RHI)] were also obtained during each 10-min cycle to sample the vertical structure of various precipitation features. Note that the *Revelle* radar beamwidth is 1.5° and its maximum unambiguous range is 150 km. The elevation angles in the PPI volume ranged from 0.8° to 21.5° in the so-called FAR mode (Fig. 1a) and from 0.8° to 35.9° in the NEAR mode (not shown), while elevation angles of the five RHI scans ranged from 0.8° to 40°. Since the number of elevation angles was kept the same between each mode, the FAR mode had higher vertical resolution and was run most of the time, while the NEAR

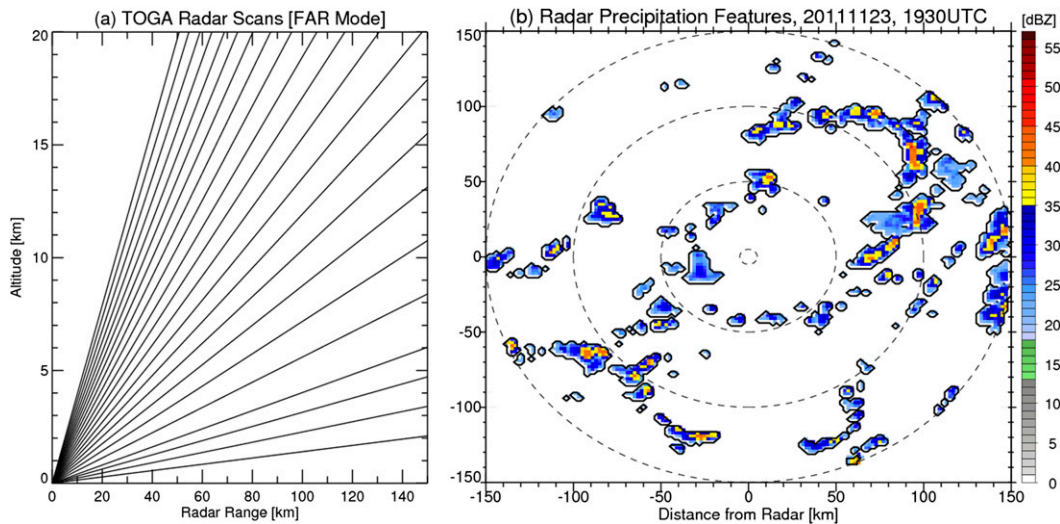


FIG. 1. Scanning strategy and measurement example of TOGA C-band radar onboard the R/V *Revelle* during DYNAMO: (a) view of all scanning-radar-beam elevation angles in the FAR mode without considering radar beam refraction and (b) an example of radar precipitation features with 20 dBZ as the boundary.

mode was taken only when deep convection was close to the radar. This particular scanning strategy was set to provide continuous volume coverage and high-resolution 3D precipitating-cloud-structure information. For example, Fig. 1a indicates that the volume scans in the FAR mode were able to detect echo tops up to 12 km in the range interval from 30 to 150 km.

The *Revelle* radar data were calibrated and quality controlled by personnel in the Radar Meteorology Group at Colorado State University and at NASA (Wallops Island). A systematic correction to the radar reflectivity of -1.5 dB was applied based on solar-gain calibrations and NASA TRMM Precipitation Radar (PR) intercomparisons. Second-trip and radio frequency (RF) noise were removed by deleting radar reflectivity without any corresponding velocity signal. Spurious echoes, skin paints from passing ships, sidelobe effects, and sea clutter were also objectively removed. Reflectivity values less than 0 dBZ was further deleted to filter weak nonraining boundaries, remaining sea clutter, and sidelobe returns. After noise filtering, radar reflectivity was corrected for attenuation A_h (dB km^{-1}) by using an A_h - Z correction procedure (Bringi and Chandrasekar 2001). The two-way A_h - Z relationship, $A_h = (9.29 \times 10^{-6}) \times Z^{0.879}$, where Z is linear reflectivity ($\text{mm}^6 \text{m}^{-3}$), was derived using disdrometer data collected at Gan Island and Manus Island (Thompson et al. 2013). Attenuation corrections were only applied to heights below 5 km, where rain can cause significant attenuation at C band. Attenuation above this level was assumed to be negligible.

After quality control, radar polar-coordinate data were interpolated to Cartesian coordinates using the

National Center for Atmospheric Research (NCAR) REORDER software package (Oye and Case 1995). The “Cressman” weighting function with an effective radius of 1.5 km was used in the interpolation process. The gridded radar data were processed to a 2-km horizontal and 0.5-km vertical grid. The 10-min output Cartesian-based radar volume covers $150 \times 150 \text{ km}^2$ horizontally and 20 km in the vertical.

2) RADAR-DERIVED PRODUCTS

Radar reflectivity was first classified into convective and stratiform precipitation components. The classification technique developed by Steiner et al. (1995) was applied to the gridded reflectivity field at 2-km altitude. Pixels with reflectivities greater than 40 dBZ are first classified as convective centers. Secondly, pixels are also defined as convective centers when they have a certain reflectivity difference [as a function of background reflectivity; the exact Eq. (2) in Steiner et al. (1995) is used here] relative to the background reflectivity. The background reflectivity is defined as the mean reflectivity of pixels within a 13-km radius from the concerned pixel. Finally, all pixels within the convective radius of those convective centers are classified as convective, while the rest of the pixels are classified as stratiform. The convective radius is a function of the background reflectivity. Here, the medium relation (or function) in Steiner et al. (1995) is adopted. Individual Z - R relationships are applied for convective and stratiform elements to derive rain rates at an altitude of 2 km. The Z - R relationship for convective rain is $Z = 130.5R^{1.45}$, and $Z = 200.46R^{1.55}$ is used for stratiform precipitation.

These relationships were derived from the same drop size distribution measurements used for the attenuation correction calculation (Thompson et al. 2013). Echo-top heights of specific echo intensities (e.g., 0 and 20 dBZ) in each grid point are obtained by finding the maximum height of that value in the gridpoint column.

Many studies have adopted echo-object techniques to investigate MJO-associated cloud population based on satellite measurements (Riley et al. 2011; Yuan and Houze 2013; Barnes and Houze 2013) and ground-based radar observations (ZH13). A particular echo-object method similar to the TRMM precipitation features (Liu et al. 2008) was applied to the entire radar dataset. Radar precipitation features (RPFs) are defined as contiguous radar pixels exceeding 20 dBZ at the 2-km height level (Fig. 1b). An RPF contains parameters such as maximum height of specific radar reflectivities (e.g., 20 or 30 dBZ), feature size (area of pixels greater than 20 dBZ), as well as intensity, area, and volume of convective and stratiform precipitation. First, RPFs are categorized by echo-top height to study the population makeup of shallow cumulus, congestus clouds, and deep convection (Johnson et al. 1999; Kikuchi and Takayabu 2004). Shallow, middle, and deep convective features are specifically defined as features with maximum height of the 20-dBZ echo less than 5 km, between 5 and 8 km, and greater than 8 km, respectively. Following DeMott and Rutledge (1998 a,b), intense convection is further categorized as RPFs with maximum height of the 30-dBZ echo greater than 8 km. In addition, RPFs are classified by size (i.e., small, medium, large) to investigate the organization of clouds across the MJO life cycle. A large feature is defined as an RPF with precipitation area larger than 1000 km², which is on the similar scale of MCSs (Liu et al. 2008). In contrast, a small feature is defined as an RPF with precipitation area smaller than 200 km². A medium feature is intermediate to these size intervals. The hourly averaged RPF number is used to calculate the daily precipitating-cloud population; for example, hourly mean is defined as the average of six radar volumes (every 10 min) rather than the total echoes observed in 1 h. RPFs smaller than 10 km² were not considered for analysis. The RPFs sampled during cruises 2–4 are listed in Table 1.

b. Sounding, SST, lightning, and TRMM data

Rawinsondes were launched every 3 h from the R/V *Revelle* as part of the DYNAMO sounding array (JC13). These soundings provided details on environmental conditions including winds, temperature, and moisture, which can be related to the radar-observed storm structures. The sounding data have approximately 150 pressure levels and were interpolated to 25-hPa increments

from the surface up to the 50-hPa level. SST data were collected from the nearby RAMA mooring (McPhaden et al. 2009) at 0°, 80.5°E. This study uses the 5-m-depth SSTs.

Lightning data collected from Vaisala's GLD360 network was used for lightning statistics. The GLD360 network detects both cloud-to-ground (CG) and some intracloud (IC) lightning by measuring the magnetic field of radio impulses generated by lightning (Said et al. 2013). GLD360 has a geolocation accuracy of less than 5 km, detection efficiency of approximately 60% for CG flashes, and a location accuracy of approximately 2.5 km (Pohjola and Mäkelä 2013; Said et al. 2013). IC flashes are detected with a lower detection efficiency (~30%; Said et al. 2010). In this study, lightning flashes within the radar range (150 km) were summed every 10 min to match the radar-volume data (10 min).

The TRMM Multisatellite Precipitation Analysis (TMPA) 3B42 rain product (Huffman et al. 2007) is used to provide a large-scale picture of rainfall over the DYNAMO array. The TMPA 3B42 dataset has 3-h temporal resolution and 0.25° × 0.25° spatial resolution. This rainfall algorithm uses TRMM PR observations, passive-microwave measurements from low-Earth-orbiting satellites, and infrared radiance measurements from geostationary satellites, as well as rain gauge data when available.

c. MJO indices

A primary goal of this study is to examine convective characteristics and environmental conditions as a function of MJO phase. We use the Wheeler–Hendon real-time multivariate MJO (RMM) index (WH index; Wheeler and Hendon 2004) to classify convective variability across the MJO life cycle. The WH index is based on the combined empirical orthogonal functions (EOFs) of OLR and zonal wind fields at 850 and 200 hPa. The WH index has been widely used and is an effective filter for intraseasonal frequencies associated with the MJO (Lau and Wu 2010; Riley et al. 2011; Barnes and Houze 2013). Based on the WH index, each day in the tropics can be assigned to one of the eight MJO phases. The active MJO phases over the CIO are assigned as phases 2 and 3. In other words, phase 1 and phase 4 correspond to preonset- and post-MJO periods in the CIO, while phases 5–8 are associated with suppressed MJO activity over the CIO. Figure 2 demonstrates the time series when R/V *Revelle* was on station as a function of WH (RMM1 and RMM2) index. During the periods of concern (October–December 2011), most of the days are in relatively strong MJO magnitudes ($\text{RMM1}^2 + \text{RMM2}^2 > 1$) indicating significant MJO events (Fig. 2). However, because of the relatively short period of the

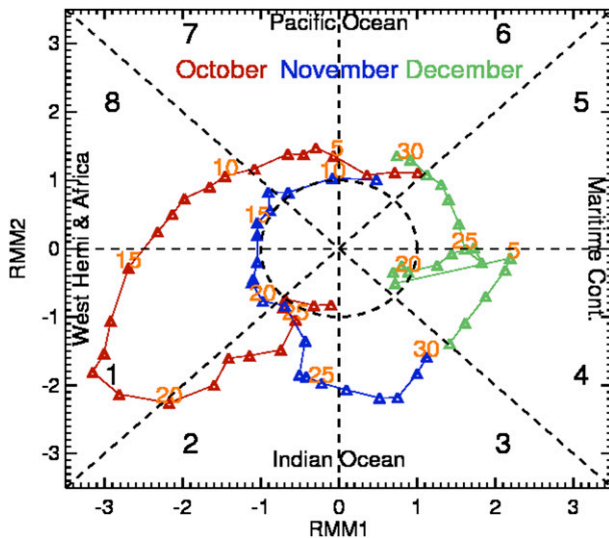


FIG. 2. Definitions of MJO phases/days from 1 Oct to 31 Dec: daily data points displayed as a function of WH index. Days are not included when the R/V *Revelle* was out of the research port.

current study, we did not exclude weak (e.g., $RMM1^2 + RMM2^2 < 1$) MJO events (Fig. 2). Accordingly, our composites are contributed from three MJO events. The October MJO (MJO 1) was observed from WH phase 6 to phase 2. The November MJO (MJO 2) was observed from phase 6 to phase 3 (Fig. 2). The December MJO (MJO 3) corresponded to WH phases 4 and 5.

The total number of samples (radar volumes) in each WH phase and contributions (fractions) from each MJO are further listed in Table 2. There are a large number of data samples in each MJO phase, which provides some confidence for the phase composites described in this study. The sample distribution is relatively uneven though; for example, radar volumes (2160) in phase 2 are about 3 times those in phase 3 (720). Most of the data samples are contributed by MJO 1 and 2, except for phases 4 and 5 when most data are contributed by MJO 3. In addition, phase 3 is only sampled in MJO 2. As a result, phases 3–5 may have larger uncertainties than other phases in our WH-index composites. However, as will be shown in section 3c, the *Revelle* radar only missed

a small amount of precipitation produced by the three MJO events. As a result, precipitation evolution (as a function of WH phase) observed by the *Revelle* radar is quite consistent with that measured by the TRMM satellite over the entire DYNAMO region.

3. Overview of MJO events during DYNAMO

a. Large-scale environmental and rainfall evolution

The DYNAMO field phase occurred during La Niña conditions when Indian Ocean SSTs were higher than climatological values (JC13). From late September 2011 to January 2012, there were two strong MJO events and one weak MJO event (Yoneyama et al. 2013; Gottschalck et al. 2013; JC13). The strong MJO 1–2 events were coherent with convection propagating to the central Pacific and corresponding wind signals circumnavigating the globe (Gottschalck et al. 2013). During MJO 1 and 2, the most enhanced convection and upper-level divergence within the Indian Ocean and western Pacific regions occurred over the DYNAMO array. MJO 3 was much weaker in the OLR field accompanied by less coherent propagation in the wind component (Gottschalck et al. 2013). In fact, MJO 3 occurred over much lower SST conditions due to extensive cooling of the upper ocean following the November MJO event (JC13; Moum et al. 2014). MJO 1 and 2 were coupled with evident Kelvin and equatorial Rossby (ER) waves, while MJO 3 experienced no coupling with Kelvin or ER waves (Gottschalck et al. 2013). Associated with these MJO events, three periods of enhanced precipitation were observed over the DYNAMO array by TRMM (Fig. 3a). MJO 1 and 2 produced heavy precipitation over the CIO with longer duration in comparison to MJO 3. This is because the CIO experienced a full MJO cycle (phases 1–8) during MJO 1 and 2 but only the decaying and suppressed phases (phases 4–6) in MJO 3 (see top axis in Fig. 3a). Multiple precipitation peaks (3–5 days) were also shown in MJO 1 and 2, probably due to the influence of the embedded Kelvin or ER waves (Gottschalck et al. 2013; JC13; ZH13).

TABLE 2. Radar data sample (radar volumes) as a function of WH MJO phase during the three MJO events. Percentages in the parentheses denote data fraction contributed from each MJO period.

	Phase							
	1	2	3	4	5	6	7	8
MJO 1	720 (56%)	1440 (67%)	0	0	0	432 (50%)	720 (62%)	720 (56%)
MJO 2	576 (44%)	720 (33%)	720 (100%)	0	0	144 (17%)	432 (38%)	576 (44%)
MJO 3	0	0	0	1728 (100%)	864 (100%)	288 (33%)	0	0
Total	1296	2160	720	1728	864	864	1152	1296

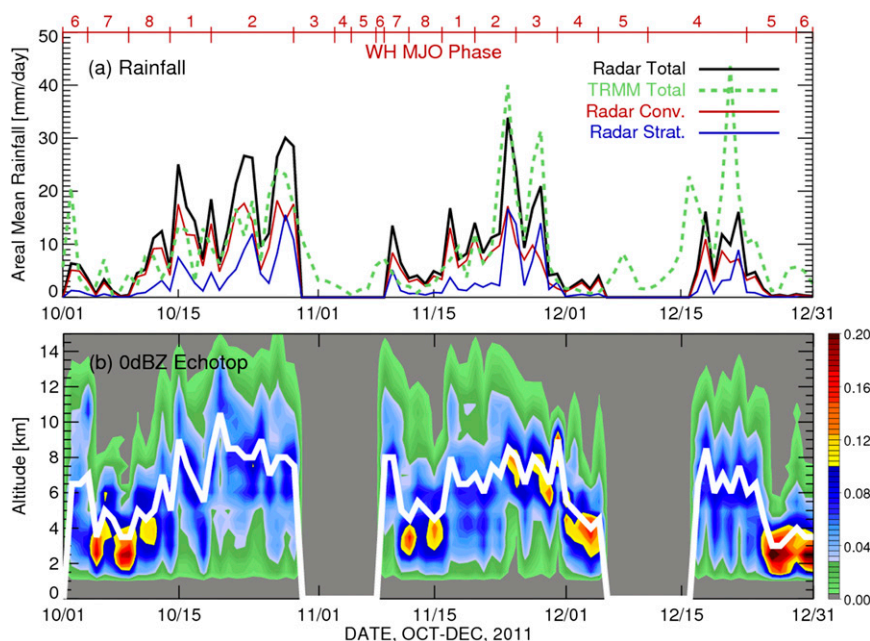


FIG. 3. Time series of (a) radar-estimated daily rainfall averaged over the radar coverage area (150-km radius) and daily rainfall derived from TRMM 3B42 over the entire DYNAMO region and (b) radar echo-top (0 dBZ) height and occurrence frequency (frequency is color shaded, while the white thick line indicates median values). Corresponding WH MJO phase numbers are indicated at the top of (a) in red numbers.

b. Evolution of precipitation and convection over the *Revelle* site

The R/V *Revelle* radar-based daily precipitation evolution was very similar to the daily precipitation observed by TRMM over the entire DYNAMO array (Fig. 3a). Furthermore, the *Revelle* rainfall analysis shows the same 3–5-day rainfall maxima within MJO 1 and 2 as the DYNAMO average from TRMM. The *Revelle* site appeared to receive less rainfall compared to that over the larger DYNAMO array (some of this difference could be due to differences in rain estimation methodologies between the ship-based radar and the TRMM 3B42 algorithm). Consistent with 3B42, the *Revelle* radar also shows that precipitation intensity in MJO 3 is much weaker than MJO 1 and 2. In MJO 1 and 2, convective rainfall dominated over stratiform precipitation before the MJO onset (phase 2), while stratiform rainfall increased substantially after onset (Fig. 3a). The echo-top (0 dBZ) evolution over the *Revelle* site clearly indicates deepening and decay of convective clouds across the MJO life cycle (Fig. 3b). The echo-top heights actually correlate very well with the precipitation total; for example, echo tops peaked (decreased) where precipitation maximized (minimized; Figs. 3a,b). Convective deepening in MJO 1 was more gradual (e.g., ~16 days from shallowest to deepest), while

MJO 2 had a somewhat more abrupt convective deepening process (~12 days). This difference is also seen in the WH index; for example, the preonset period (phases 7–1) in MJO 1 is 16 days—5 days longer than that MJO 2 (Fig. 2). In fact, the more abrupt MJO onset process of MJO 2 in comparison to MJO 1 was also seen in more rapid tropospheric moistening, SST warming, and low-level convergence (JC13).

c. *Revelle* observations compared to TRMM measurements

This subsection aims to justify the radar observations (i.e., precipitation total) over the *Revelle* in analyzing MJO evolution through comparison to TRMM estimates (3B42) over the larger DYNAMO area. Two different levels of comparisons are conducted. First, daily evolution of radar-estimated rainfall is compared with that of the TRMM rainfall over the entire DYNAMO area (Fig. 3a). Second, WH-composited evolution of the *Revelle* radar-estimated rainfall is compared to TRMM rainfall over the entire DYNAMO array (8°S–6°N, 72°–80°E), the northern sounding array (NSA; 0°–6°N, 72°–80°E), the southern sounding array (SSA; 8°S–0°, 72°–80°E), and the *Revelle* radar coverage area (Fig. 4).

Based on the time series analysis (Fig. 3a), the *Revelle* radar observed the bulk of the precipitation produced by the three MJO events. The missing observations were

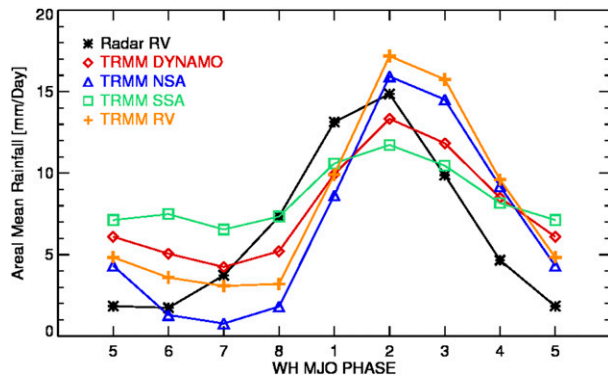


FIG. 4. Rainfall composites as a function of WH MJO phase. Radar-estimated rainfall is derived over the radar coverage area (*Revelle* radar, black) during the R/V *Revelle* operation time period. TRMM-based rainfall is derived during October–December over the entire DYNAMO region (DYNAMO, red), the northern sounding array (TRMM NSA, blue), southern sounding array (TRMM SSA, green), and the *Revelle* radar area (1.5°S – 1.5°N , 79° – 82°E) (TRMM RV, orange).

during relatively dry periods when the *Revelle* was off station (e.g., 30 October–7 November, 6–15 December) after each MJO active period. The daily rainfall around the *Revelle* site is also very similar to that of the average over the entire DYNAMO region. For example, radar-based rainfall analysis shows most of the rainfall peaks and minima observed by TRMM. More importantly, the WH-composited rainfall evolution observed by the *Revelle* radar is generally consistent to that measured by the TRMM over larger area in the CIO (Fig. 4). For example, each rainfall analysis shows a similar increasing trend from phase 7 to phase 2, maximum at phase 2, and a decreasing trend from phases 2 to 5. This indicates that the *Revelle* measurements captured very well the major MJO signals. This is very possibly due to the high temporal sampling (round the clock) of the radar operations.

It is important to note that the three MJO events have differences. The most distinct difference between MJO 1 and 2 is the onset timing. The onset of MJO 2 is much more rapid than MJO 1, as seen from the increasing echo-top heights (Fig. 3b) and the tropospheric moistening (JC13). However, compositing MJO events by WH index already includes the duration difference of the onset process among different MJOs; for example, the WH index also indicates that preonset phases are longer in MJO 2 than in MJO 1 (Fig. 2). Of course, MJO 3 did not even initiate over CIO region, having only phases 4 and 5 over the CIO. Compositing phases 4 and 5 in MJO 3 into MJOs 1 and 2 might not truly represent the decaying periods of these MJOs. This limitation will be stressed in interpreting our results.

4. Results based on global WH index

a. Environmental conditions and convective characteristics

Figure 5 displays general environmental conditions at/near the R/V *Revelle* as well as the radar-determined surrounding ($300 \times 300 \text{ km}^2$) convective characteristics, all as a function of WH MJO phase. A simple 1–2–1 smooth filter was applied to these time series. These composites show coherent increasing transitions from suppressed phases to active phases and decreasing transitions after active MJO periods. As we discuss below, the temporal behavior of our observations resemble the recharge and discharge processes in the recharge–discharge MJO theory (Bladé and Hartmann 1993; Hu and Randall 1994; Kemball-Cook and Weare 2001). Basically, both environmental conditions (e.g., total precipitable water, CAPE, and SST; Fig. 5a) and convective activity (e.g., echo top, precipitation, and lightning; Fig. 5b) achieve minimal values in the CIO during WH phases 5–6, while they achieve near peak values in phases 1–2. During phases 5–6, the atmosphere is relatively dry and stable, and the upper ocean is relatively cool. As a result, convection, as indicated by echo-top heights and rainfall, is the most suppressed in these periods over the CIO, allowing the upper ocean to warm due to enhanced solar insolation, reduced cloudiness, and light winds (resulting in greatly reduced upper-ocean mixing; Moum et al. 2014). As a consequence, the atmosphere begins to recharge with increasing CAPE and moistening. These processes lead to the growth of convection (Fig. 5b). During phases 5–8, the atmospheric moistening occurs mainly at the lower levels (e.g., 925–700 hPa).

By phase 1, SSTs reach peak values, and resultant low-level heating and moistening of the lower atmosphere produce high values of CAPE (Fig. 5a). Note that CAPE actually peaks in phase 8 even though SST is highest in phase 1, suggesting that CAPE is consumed by the growing convective population in phase 1. However the isolated nature of convection in phase 1 is such that SSTs can still increase. In phase 1, radar echo-top heights and lightning frequency (indicative of convective strength) reach their maximum values (Fig. 5b). The lightning peak in phase 1 correlates well with CAPE, as has been demonstrated in many previous studies regarding tropical convection (e.g., Rutledge et al. 1992; Williams et al. 1992). Based on TRMM satellite measurements, Morita et al. (2006) also showed that lightning frequency peaks before the MJO active phase. Though convective intensity peaks in phase 1, total column moisture (Fig. 5a) and precipitation (Fig. 5b) both peak one phase later. Convection in phase 1 also produces much less stratiform

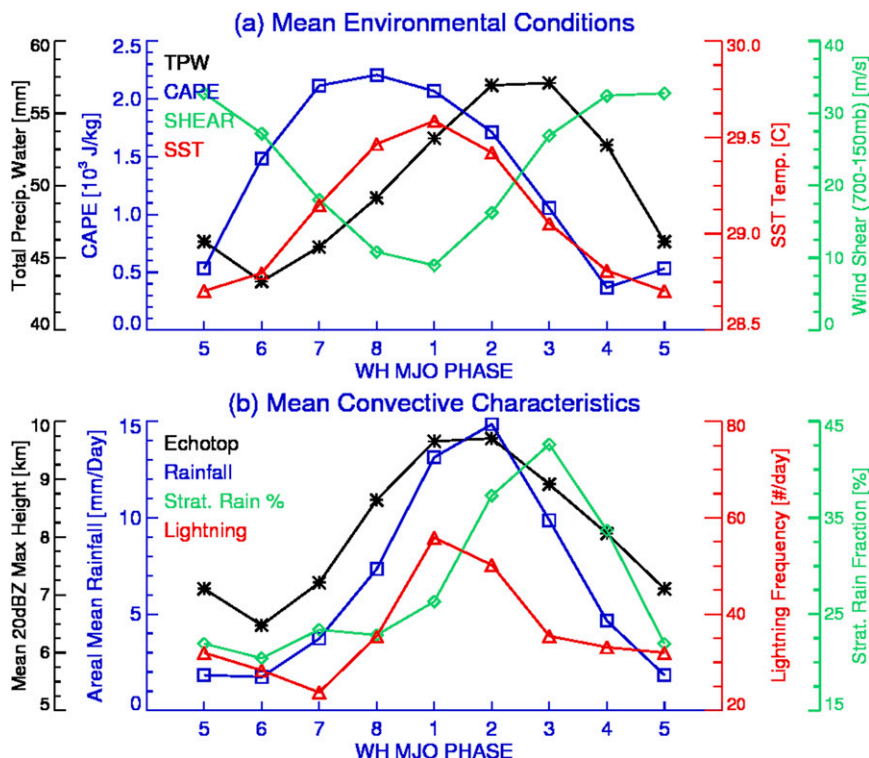


FIG. 5. WH MJO phase-to-phase composites: (a) environmental conditions observed at the ship site, including the total precipitable water (TPW, black), CAPE at 1500 LT (blue), 700–150-hPa wind shear (green), and SST at 5-m depth (red) and (b) radar-measured convective characteristics within 150-km radius, including maximum 20-dBZ echo-top height averaged by all 10-min radar volumes (black), areal-mean daily rainfall (blue), stratiform precipitation fraction (green), and lightning frequency (red).

precipitation compared to phase 2 (later we will show that the convection in phase 1 is more isolated). The mid- to upper troposphere only begins to moisten at phase 1. The convective depth (20-dBZ echo-top height) indeed leads the mid- to upper-tropospheric moisture by two phases, indicating the probable role of deep convection in moistening the mid- to upper troposphere.

Total column moisture and precipitation do not maximize until the MJO onset (phase 2; Fig. 5a). During phase 2, precipitation systems are both deep and organized (with an attendant large fraction of stratiform precipitation, approximately 40%; Fig. 5b) as the environments are favorable for such (high CAPE to support deep convection, a moist troposphere, and significant deep shear, as shown in Fig. 5a). Moist mid- to upper-tropospheric conditions are favorable for stratiform precipitation growth (Tao et al. 1993; Halverson et al. 1999), while strong environmental shear can help produce broad stratiform areas (Saxen and Rutledge 2000; Shie et al. 2003; Lin et al. 2004). When the MJO active phase transitions to phase 3, radar echo tops and rainfall decrease substantially (Fig. 5b), coupled with a decrease

in both SST and CAPE (Fig. 5a). Though convective intensity weakens significantly in phase 3, stratiform precipitation continues to blossom and achieves the largest contribution to rain volume (approximately 45%). Large stratiform precipitation fractions in active MJO phases have been previously quantified using TRMM data (Lin et al. 2004). Lin et al. 2004 showed that the stratiform rain fraction is about 10% higher during active MJO periods compared to annual-mean values (40%–50%) over the eastern Indian Ocean and western Pacific. The higher stratiform fraction is consistent with larger wind shear (Fig. 5b) and moist conditions in the mid- to upper troposphere (Fig. 6), as found in previous studies (Saxen and Rutledge 2000; Shie et al. 2003; Lin et al. 2004; Lin and Mapes 2004). During the 1992/93 TOGA COARE experiment, stratiform rain fractions were in phase with both low-level (1000–850 hPa) and deep (700–150 hPa) shear (Lin et al. 2004). The stratiform rain fraction and wind shear maxima lagged the heaviest precipitation by about 5–10 days (Lin et al. 2004).

The lower troposphere begins to dry at phase 3, even though the upper troposphere is characterized by peak

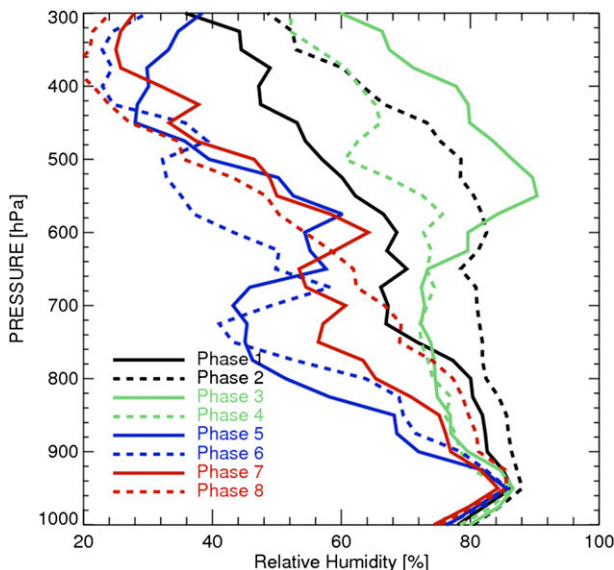


FIG. 6. Composites of relative humidity vertical profiles as a function of WH MJO phase based on the soundings launched from R/V *Revelle*.

values in relative humidity at this time (Fig. 6). After the MJO convective envelope propagates to the east of the CIO (phase 4), convective vigor, precipitation, humidity, and instability in the DYNAMO area all decrease remarkably (Fig. 5b). Upper-level drying by subsidence in the wake of the deep convection is quite evident (Fig. 6), as are decreases in SST and CAPE (Fig. 5a). Lowering of the SST associated with these MJO events has been recently discussed by Moum et al. (2014). Four factors contributed to the sharp reduction in SST: reduction in solar insolation due to cloudiness, widespread rainfall, the entrainment of cooler subsurface water to the ocean surface due to shear driven mixing, and enhanced heat fluxes out of the ocean.

b. Precipitating-cloud population

This section examines the specific makeup of the precipitating-cloud (or RPF) population across the MJO cycle during DYNAMO. In general, the RPF population (Fig. 7) evolves similarly to convective depth (20-dBZ echo top) and total precipitation as shown in the last section (Fig. 5b). The total RPF population grows to a significant level before the MJO onset (phases 8–1), peaks at phase 2 when the rainfall amount reaches its maximum, then diminishes rapidly to suppressed periods (phases 5–6). The RPF population difference between the peak ($\sim 1000 \text{ day}^{-1}$) and the minimum ($\sim 150 \text{ day}^{-1}$) is substantial. The active MJO period (phases 2–3) in the CIO not only has more deep precipitating clouds but also more shallow and middepth

precipitating clouds compared to the suppressed phases (phases 5–7; Fig. 7a). It is interesting that shallow convection is ubiquitous, occupying roughly 40%–50% of the total population throughout the MJO life cycle (Fig. 7a). Though the CIO RPF population in the pre-onset phase (e.g., phase 8) is similar to that of the active phase (phase 2), it is composed of a higher fraction of small (or isolated) features compared to the active phase (Fig. 7b).

Figure 7 breaks down the RPF population into specific convective types. Growth of shallow and isolated convection from the suppressed to preonset period is quite evident (Figs. 8a,b). The total number of shallow isolated RPFs maximize in phase 8, two phases prior to the MJO onset over the CIO (phase 2). The RPF population correlates very well with the lower (850–700 hPa) tropospheric humidity (Fig. 8a) and CAPE (Fig. 5a). This indicates the probable role of shallow cumulus in moistening the lower troposphere (Benedict and Randall 2007; Lau and Wu 2010; Del Genio et al. 2012). Deep convection in phase 8 is still fairly suppressed (Fig. 8c), likely attributable to dry mid- to upper-tropospheric conditions in this phase (leading to strong entrainment and convective dilution), even though CAPE peaks in this phase. With the inhibition of deep convection, MCSs in this phase are also rare (large RPFs; Fig. 8d). On the other hand, the population of deep convection maximizes in phases 1–2. Deep convective cells in phase 1, however, develop into large features (or MCSs) less frequently than those in phase 2 (Figs. 8c,d), yet the cells in phase 1 are the most vertically intense convective cores (30-dBZ echo top greater than 8 km; Fig. 8e) observed throughout the MJO envelope. The population of intense convection (Fig. 8e) displays a similar pattern as the lightning frequency (Fig. 5b). Hence this lightning peak over the MJO phase denotes the period of strongest convection, which is in the form of intense, mostly isolated convective cells.

With the onset of the MJO over the CIO (phase 2), convectively deep and large precipitating systems become more frequent (Figs. 8c,d). Actually, there are about 80% more large features (at the MCS scale) occurring in phase 2 than in phase 1, indicating the more organized nature of convection in the active phase (Fig. 8d). This radar-based finding well matches the satellite-based finding that deep narrow (or isolated) convection is more prevalent during preonset MJO periods, while wide (or organized) convection is more common during active periods (Morita et al. 2006; Tromeur and Rossow 2010; Riley et al. 2011). Though the deep convective population decreases more than 40% when the active phase evolves to phase 3 (Fig. 8c), large precipitating systems are still prevalent (Fig. 8d). As shown in section

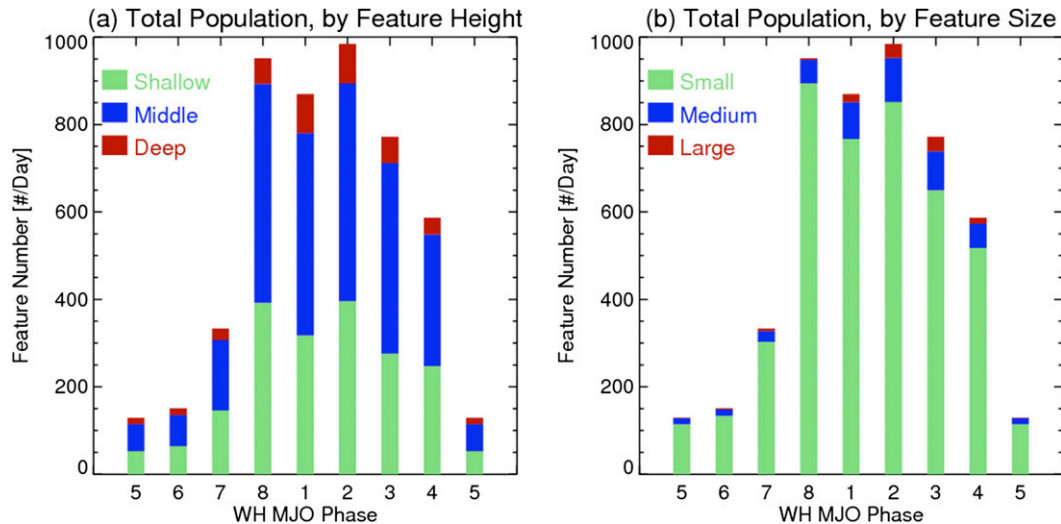


FIG. 7. Histograms of precipitating-cloud population (RPFs) as a function of WH MJO phase: (a) total population categorized by feature height (maximum 20-dBZ echo top) and (b) total population classified by feature size.

3a, these large systems have significant fractions of stratiform precipitation (Fig. 5b). In short, phases 1–3 show signatures that resemble the developing, mature, and decaying stages, respectively, of an individual MCS (Mapes et al. 2006). This behavior is consistent with relatively dry mid- to upper-tropospheric conditions and reduced shear in phase 1, while moist and significant shear conditions in active phase (phases 2–3) promote the growth of stratiform precipitation (Tao et al. 1993; Houze 2004).

Examples of the radar echo patterns in each MJO phase are shown in Fig. 9. These examples summarize the descriptions of convection across the MJO life cycle and are similar to the evolution of an individual MCS (Mapes et al. 2006; Morita et al. 2006; Riley et al. 2011). Indeed, ZH13 documented this same similarity for the DYNAMO convective population but for the 2–4-day heavy rainfall episodes. During the most suppressed conditions in the CIO (phases 5–6), convection is infrequent (Fig. 9a). The convection that does form remains primarily isolated (Fig. 9a). In phases 7–8, shallow, isolated convection is common and often distributed throughout the entire radar coverage area (Fig. 9b). Phase 1 is characterized by isolated deep and intense convection (Fig. 9c). During this phase, the troposphere is favorable for intense convection with significant CAPE (Fig. 5a). With the onset of the MJO (phase 2; Fig. 9d), deep convective cells start to develop into organized (including large) MCSs, and stratiform precipitation increases substantially as the upper-tropospheric humidity increases (Fig. 6). Through examination of the *Revelle* radar images, MCSs in phase 2 are found to be in the form of both leading convective–trailing

stratiform and embedded convection within stratiform precipitation. As the active MJO event evolves into phase 3 (Fig. 9e), convection becomes somewhat weaker in response to diminishing CAPE and SST. Precipitating clouds in this phase exhibit extremely large stratiform areas, with stratiform rainfall fractions approaching 45% (Fig. 5b). During the transition phase (phase 4), precipitation is still significant but the convection is weaker and less organized (Fig. 9f). Data samples from phase 4 are limited to MJO 3, so the convective population for this phase needs to be interpreted with caution because of the reduced number of samples.

c. Precipitation structure and contribution by cloud types

This section further investigates MJO precipitating clouds in terms of their structure and rainfall contributions based on RPFs. RPFs are defined as clusters of radar echoes exceeding 20 dBZ; therefore, the precipitation that falls from raining areas less than 20 dBZ (~5% of total rainfall) is ignored for this analysis. The frequency of precipitation occurrence [probability density function (PDF)] is displayed as a function of both precipitating-cloud height (20-dBZ echo top) and precipitation area (Fig. 10). The mean joint PDF across all MJO phases shows a combination of three distinct precipitation structures (Fig. 10a): “bottom heavy” (shallow cumulus), “middle heavy” (large stratiform with weak convection), and “top heavy” (deep convection). Each individual MJO phase is generally dominated by one of these precipitation structures. For example, the suppressed MJO phases (phases 6–8) display mostly a bottom-heavy structure and a much

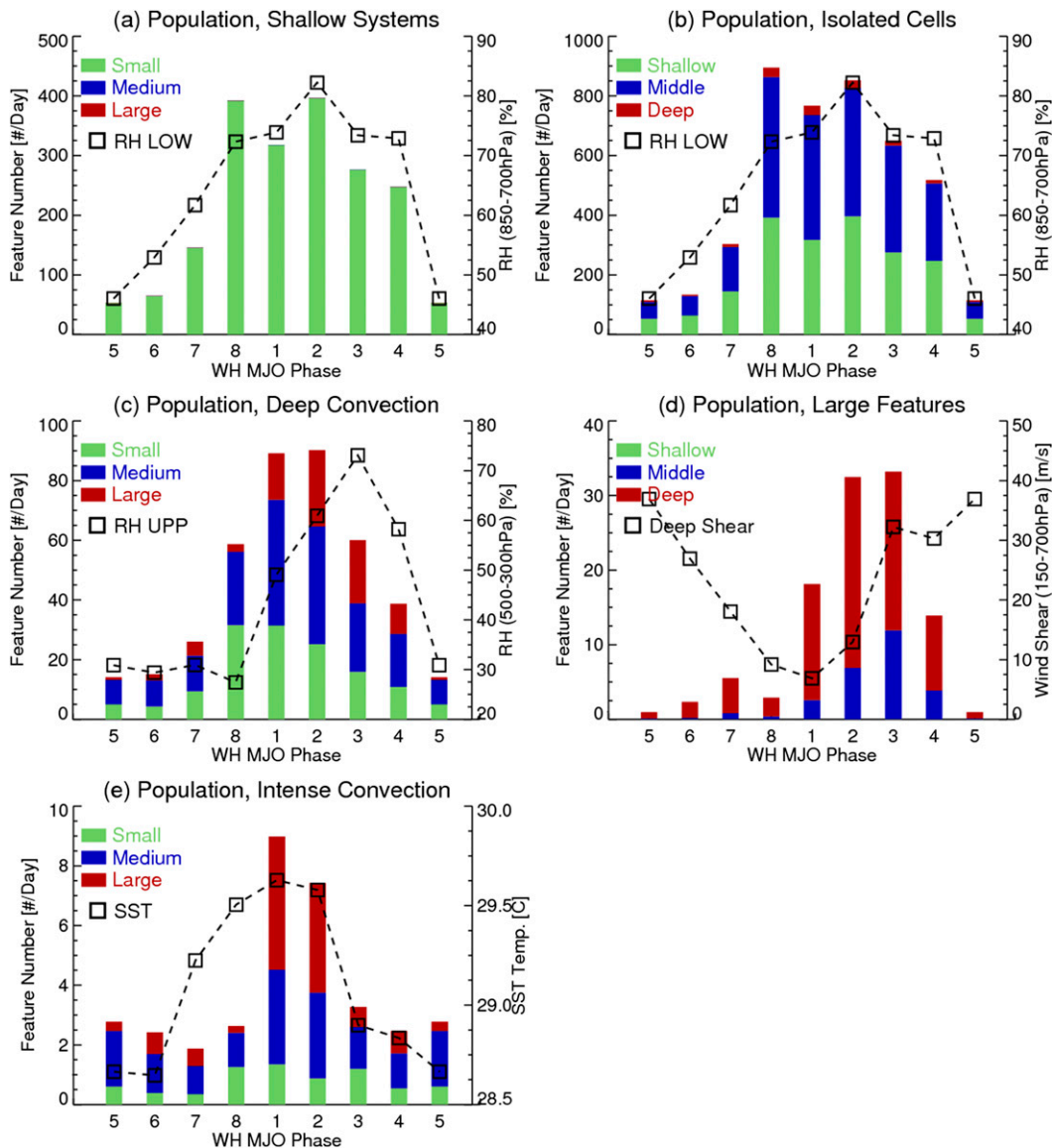


FIG. 8. Population of specific group of RPFs as a function of WH MJO phase: (a) shallow systems with breakdowns into small, medium, and large; (b) isolated cells with breakdowns into shallow, middle, and deep; (c) deep convection with breakdowns into small, medium, and large; (d) large features with breakdowns into shallow, middle, and deep; and (e) intense convective cells with breakdowns into small, medium, and large. Low-level (850–700 hPa) RH, mid-to upper-level (500–300 hPa) RH, deep shear (700–150 hPa), and 5-m-depth SST are overlapped in (a) and (b), (c), (d), and (e), respectively.

narrower distribution (Figs. 9b–e). During these periods, echo-top height and precipitation area are highly correlated, indicating that precipitation area increases as the depth of the convection increases. The transition from phase 7 to 8 is slightly discontinuous where large features developed in phase 7 but not phase 8 (Figs. 10d,e). Those small number of large precipitation systems in phase 7 (Fig. 8d) might be due to propagation from the east or off the equator or caused by wave disturbances (e.g., Kelvin wave; Gottschalck

et al. 2013; JC13). Phases 1 and 2 exhibit a top-heavy feature that has a large fraction of precipitation falls from systems that are deep (>8 km) with large precipitation areas (Figs. 10f,g). The middle-heavy distribution is noted in phases 3–4, with echo tops in the 5–8-km range over a broad range of raining areas (Figs. 10h,i). This is consistent with the more stratiform nature of the precipitation in these phases. These large stratiform areas are associated with shallower convection compared to phases 1–2. Lau and Wu (2010) showed

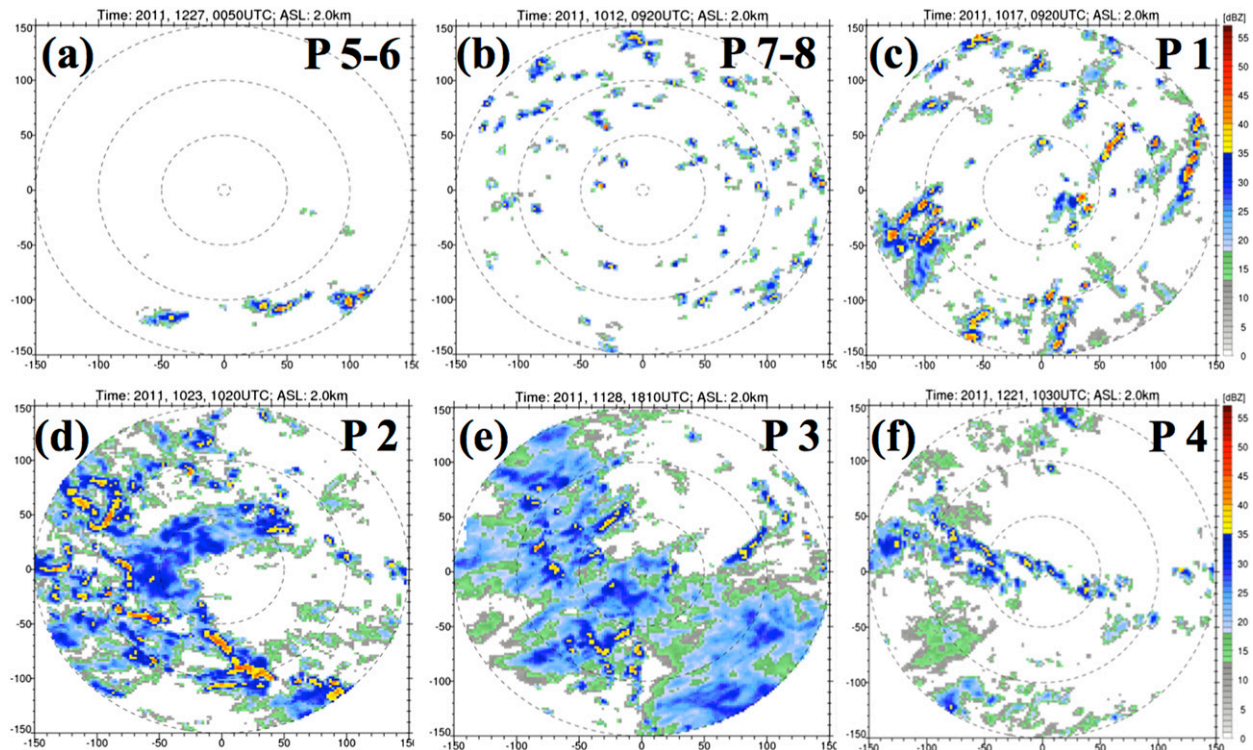


FIG. 9. Radar reflectivity at 2 km of typical case of precipitating systems (RPFs) at each WH MJO phase: (a) phases 5–6, (b) phases 7–8, (c) phase 1, (d) phase 2, (e) phase 3, and (f) phase 4.

a similar bottom-heavy precipitation structure in suppressed MJO periods and top-heavy distributions for active phases based on long-term TRMM analysis. Similar cloud structures across the MJO life cycle are also indicated by satellite pixel-based statistics (Riley et al. 2011). These phase-to-phase transitions in precipitation structure are consistent with convective characteristics shown in previous sections and earlier studies.

It is also important to quantify the rainfall production of various precipitating-cloud types (Rickenbach and Rutledge 1998). Figure 11 shows both the precipitation area and precipitation amount contributed from different types of radar echoes. Again, the most active phase (e.g., phase 2) has the largest total precipitation area and amount, while the most suppressed period (e.g., phases 5–6) has the least. Precipitation accumulation increases as the MJO transitions from suppressed, to preonset phases (phases 8–1), to active phases (phases 2–3). Though phase 1 contains similar total and deep precipitating-cloud populations as phase 2 (Fig. 7), phase 1 produces much less total precipitation area ($\sim 50\%$ less; Fig. 11a), suggesting precipitation systems prior to MJO onset are more isolated in nature. Shallow convection contributes very little to the total precipitation (both area and amount) throughout the MJO cycle (Figs. 11a,b),

even though their frequency of occurrence is high in all MJO phases (Fig. 7). We suggest that shallow convective cells play an important role in preconditioning the lower atmosphere for subsequent deep convection (especially during phases 7 and 8). During all phases, systems with echo tops reaching only the middle levels (5–8 km) contribute nearly equally to precipitation area compared to deep systems (Figs. 11a,b). A nonnegligible fraction (10%–15%) of rainfall comes from small systems across the MJO cycle, especially during the suppressed phases (Figs. 10c,d) when small convective clouds dominate (Fig. 7b). For example, 70% of the rainfall in phase 8 falls from small isolated convective cells—cells with echo tops at or below 5 km MSL (Fig. 10d). During MJO active periods, large MCSs contribute more than 70% of the total precipitation, which is similar to findings from TOGA COARE (Rickenbach and Rutledge 1998).

5. Summary and discussion

a. Summary

This study used DYNAMO shipborne radar observations combined with atmospheric soundings, lightning, and SST data to investigate convective and environmental conditions associated with MJO life cycle over the

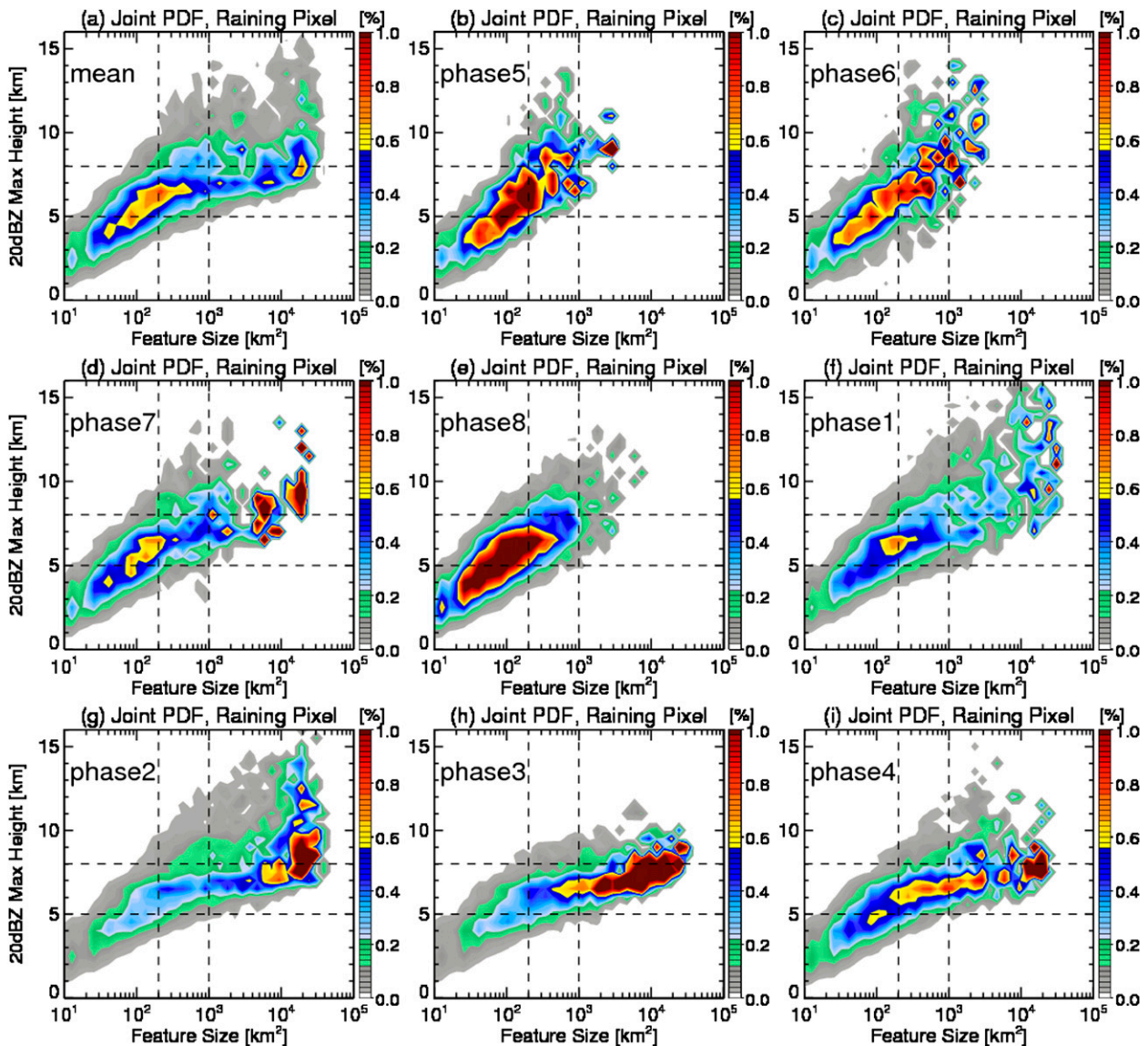


FIG. 10. Joint PDFs of precipitation area as a function of both echo-top height (20 dBZ) and size of precipitating systems (RPFs): (a) mean PDFs of all WH MJO phases and (b)–(i) specific WH MJO phases. Horizontal dashed lines mark shallow (5 km) and deep (8 km) echo-top heights, while vertical dashed lines mark small (200 km²) and large (1000 km²) areas.

CIO. We use statistics of both echo objects (or features) and gridded radar pixels to explore precipitation morphology, convective intensity, rainfall contributions, and lightning frequency throughout the MJO life cycle. This study complements satellite-based (e.g., TRMM and *CloudSat*) studies, as it examines the MJO convection from the continuous evolution perspective rather than satellite snapshots. Our results can be used to evaluate the MJO model simulations, for example, to ensure that the models capture similar quantitative convective properties and the evolution of the precipitating cloud population across the MJO life cycle. The evolution of the MJO convective population and environmental

conditions generally support the “recharge–discharge” MJO conceptual model reported in the literature. Results from this study can be summarized as follows:

- 1) There is an evident stepwise transition of the total population of precipitating clouds throughout the MJO; all types of precipitating clouds occur to some extent, but the relative frequency of each type varies with MJO phase.
- 2) Convective populations in the suppressed periods (phases 5–6) are minimal and dominated by shallow and isolated convective cells; as SST and CAPE increase, shallow and isolated convective cells

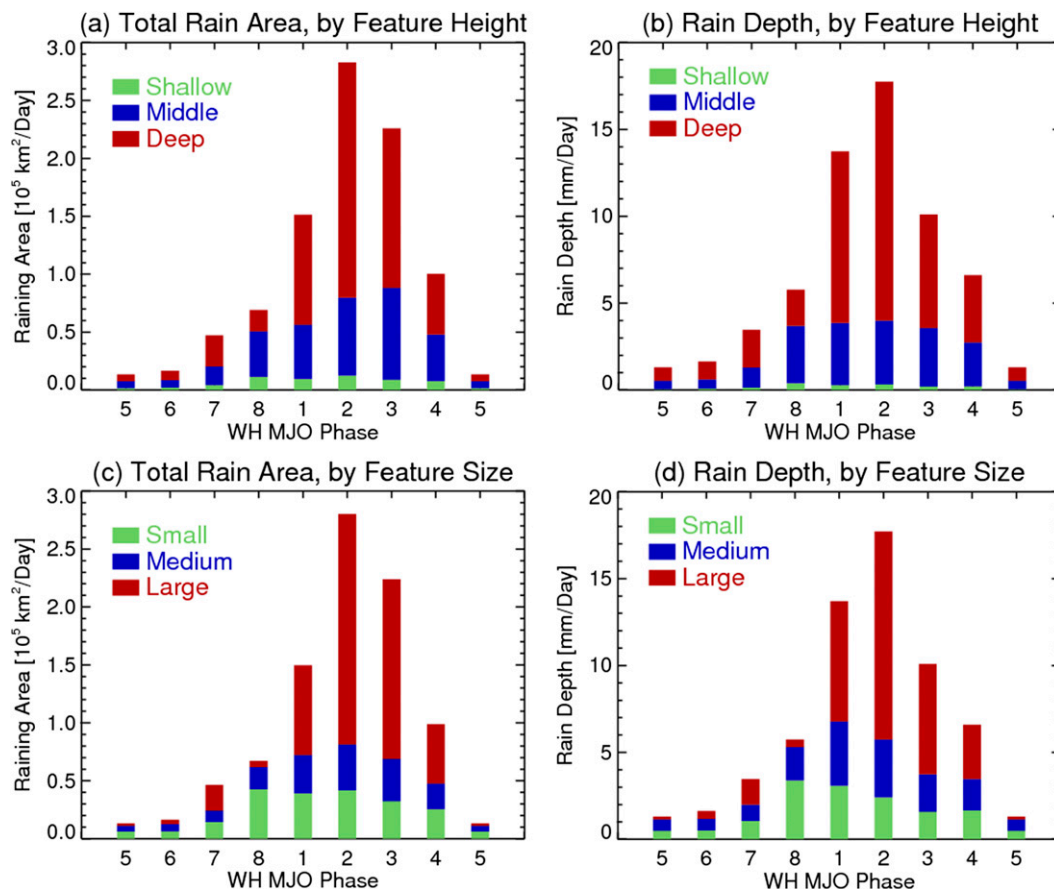


FIG. 11. Precipitation contribution by (a),(b) feature height and (c),(d) feature size. (left) Total precipitation area contributed by different types of storms and (right) areal-mean rainfall (rain depth).

become more frequent and peak in phase 8, followed by the lower-tropospheric (850–700 hPa) humidity (moistening).

- 3) The frequency of deep and intense convection (accompanied by maximum lightning activity) peaks at phase 1, one phase prior to the MJO onset; these deep convective systems are limited in horizontal extent and produce relatively small amounts of stratiform precipitation; the population of deep convection leads the humidity (moistening) at mid- to upper levels (500–300 hPa) by one to two phases.
- 4) During phase 2 (MJO onset), deep convection can grow upscale into organized MCSs producing substantial amounts of stratiform precipitation, although convective intensity and lightning frequency is reduced compared to phase 1; the mid- to upper troposphere further moistens, and the SST begins to decrease owing to heavy precipitation and extensive cloudiness and upper-ocean mixing driven by low-level westerly winds.

- 5) In phase 3, precipitating systems are characterized by large stratiform precipitation fraction ($\sim 45\%$) accompanied by much weaker convective cores; mid- to upper levels are moistened to peak values in this phase, although the lower to midtroposphere begins to dry; deep wind shear becomes more pronounced ($>25 \text{ m s}^{-1}$).

b. Discussion

The precipitating-cloud population composited across the MJO life cycle resembles the evolution of an individual MCS, but on a much longer time scale and over a greater area. In fact, this cloud-transition pattern has also been found by long-term satellite snapshot statistics (Morita et al. 2006; Riley et al. 2011; Barnes and Houze 2013), model reanalysis (Benedict and Randall 2007), and measurements from field campaigns (Lin and Johnson 1996; JC13). ZH13 showed this MCS-like evolution on a shorter (2–4 days) time scale by compositing heavy-rainfall episodes during DYNAMO. This resemblance of the precipitating-cloud evolution across

different time and space scales to the individual MCS life cycle is proposed as the “stretched building block” mechanism by [Mapes et al. \(2006\)](#). The cloud population is hypothesized to occur through a stretched building block conceptual model, in which the widths (durations) of zones of shallow, deep, and stratiform clouds in MCSs are modulated by larger-scale wave disturbances. At any given MJO period, all types of precipitating clouds occur (e.g., shallow isolated, isolated deep, large stratiform, etc.), but their relative frequencies maximize at different stages of the MJO life cycle for particular type. The large-scale environment during each MJO period determines how deep and how large individual precipitation features can become. For example, the relative dry and stable environment in the suppressed period results in most of the convective cells being shallow and isolated; however, a small number of cells do develop into deep convective cells. The preonset periods are characterized by high CAPE, moist low levels, dry mid- to upper levels, and reduced wind shear. This environment favors a population of deep and intense convective elements but not organized MCSs with large stratiform precipitation areas. In contrast, the troposphere is sufficiently moist and unstable in the active MJO periods, which allows convective elements to grow upscale at upper levels, forming a significant amount of stratiform precipitation. At the later part of the MJO active period, instability of the environment is reduced substantially and so is convective vigor. But the remaining moist conditions in the presence of deep vertical wind shear support a large fraction of stratiform precipitation.

This study indicates that shallow isolated and deep convection leads the lower- and mid- to upper-level moistening, respectively. This behavior indicates the potential role of convective moistening in the MJO initiation process. In short, a series of processes may occur during the MJO initiation (or “recharge”) period. First of all, the remarkable increase of shallow isolated cumulus clouds moistens the lower levels. The moist lower troposphere combined with high SST and/or CAPE supports the development of isolated deep convection, although the mid- to upper troposphere is still relatively dry. However, the deep convection promotes rapid moistening of the mid- to upper troposphere through cloud detrainment or vertical advection of moist static energy. Based on TRMM statistics, [Barnes and Houze \(2013\)](#) and [Yuan and Houze \(2013\)](#) also suggested that deep convective cells contribute to continuous mid-tropospheric moistening.

This study also shows that the strongest convective cores were present prior to the MJO onset, consistent with previous studies ([DeMott and Rutledge 1998a,b](#); [Morita et al. 2006](#); [Riley et al. 2011](#)). These intense

convective cells are indeed supported by an environment with maximum values of SST and CAPE. Furthermore, we speculate that invigoration of convection by changing aerosol concentrations ([Williams and Stanfill 2002](#); [Yuan et al. 2011](#); [Tao et al. 2012](#)), although out of the scope of this study, may also contribute to the enhanced convective intensity and lightning activity prior to the MJO onset. [Dewitt et al. \(2013\)](#) found a high concentration of small aerosols in the lower atmosphere just prior to the active MJO during DYNAMO. It is possible that these high aerosol (CCN) concentrations could have acted to reduce coalescence growth and promote robust mixed-phase processes, allowing the release of latent heat via freezing to further invigorate convective updrafts ([Williams and Stanfill 2002](#)). On the other hand, [Dewitt et al. \(2013\)](#) showed that the active phase has a “green ocean-like” aerosol environment (larger aerosols in much reduced concentrations compared to the onset phase). This latter situation is more favorable for “warm rain” processes ([Williams and Stanfill 2002](#)), which act to reduce the intensity of the mixed phase.

Acknowledgments. This research was supported by the National Science Foundation DYNAMO Project Grant AGS-1063928. We acknowledge Brenda Dolan, Elizabeth Thompson, Timothy Lang, and Paul Hein for radar data quality control and processing help. We thank Elizabeth Thompson and Brenda Dolan for scientific discussions. We also thank Richard Johnson and Paul Ciesielski for sounding data support and science discussions, Carl Schreck for providing the MJO-filtered TRMM rainfall data, and Vaisala Inc. for providing the GLD360 lightning data. We are grateful for radar operations support from many scientists, engineers, and students from NASA, Colorado State University, and University of Hawai‘i at Mānoa. We thank the entire crew of the R/V *Revelle* for their excellent support and *Revelle* Chief Scientist James Moum for his dedication and leadership. We are also grateful to Robert Houze and Courtney Schumacher and their research groups for numerous discussions regarding the planning of the radar component for DYNAMO, subsequent data analysis, and science discussions. Finally, we thank Ramesh Kakar, Arthur Hou, John Gerlach, and Walter Petersen (all NASA) for making the NASA TOGA radar available for DYNAMO. Chidong Zhang was the lead PI for DYNAMO and we are grateful for his excellent leadership of the project.

REFERENCES

- Barnes, H. C., and R. A. Houze Jr., 2013: The precipitating cloud population of the Madden–Julian Oscillation over the Indian and west Pacific Oceans. *J. Geophys. Res. Atmos.*, **118**, 6996–7023, doi:10.1002/jgrd.50375.

- Bechtold, P., M. Köhler, T. Jung, F. Doblas-Reyes, M. Leutbecher, M. J. Rodwell, F. Vitart, and G. Balsamo, 2008: Advances in simulating atmospheric variability with the ECMWF model: From synoptic to decadal time-scales. *Quart. J. Roy. Meteor. Soc.*, **134**, 1337–1351, doi:10.1002/qj.289.
- Benedict, J. J., and D. A. Randall, 2007: Observed characteristics of the MJO relative to maximum rainfall. *J. Atmos. Sci.*, **64**, 2332–2354, doi:10.1175/JAS3968.1.
- , and —, 2009: Structure of the Madden–Julian oscillation in the superparameterized CAM. *J. Atmos. Sci.*, **66**, 3277–3296, doi:10.1175/2009JAS3030.1.
- Bladé, I., and D. L. Hartmann, 1993: Tropical intraseasonal oscillations in a simple nonlinear model. *J. Atmos. Sci.*, **50**, 2922–2939, doi:10.1175/1520-0469(1993)050<2922:TIOIAS>2.0.CO;2.
- Bringi, V. N., and V. Chandrasekar, 2001: *Polarimetric Doppler Weather Radar: Principles and Applications*. Cambridge University Press, 664 pp.
- Chen, S. S., R. A. Houze Jr., and B. E. Mapes, 1996: Multiscale variability of deep convection in relation to large-scale circulation in TOGA COARE. *J. Atmos. Sci.*, **53**, 1380–1409, doi:10.1175/1520-0469(1996)053<1380:MVODCI>2.0.CO;2.
- Del Genio, A. D., Y. Chen, D. Kim, and M.-S. Yao, 2012: The MJO transition from shallow to deep convection in *CloudSat*/CALIPSO data and GISS GCM simulations. *J. Climate*, **25**, 3755–3770, doi:10.1175/JCLI-D-11-00384.1.
- DeMott, C. A., and S. A. Rutledge, 1998a: The vertical structure of TOGA COARE convection. Part I: Radar echo distributions. *J. Atmos. Sci.*, **55**, 2730–2747, doi:10.1175/1520-0469(1998)055<2730:TVSOTC>2.0.CO;2.
- , and —, 1998b: The vertical structure of TOGA COARE convection. Part II: Modulating influences and implications for diabatic heating. *J. Atmos. Sci.*, **55**, 2748–2762, doi:10.1175/1520-0469(1998)055<2748:TVSOTC>2.0.CO;2.
- DeWitt, L. H., D. J. Coffman, K. J. Schulz, W. A. Brewer, T. S. Bates, and P. K. Quinn, 2013: Atmospheric aerosol properties over the equatorial Indian Ocean and the impact of the Madden-Julian oscillation. *J. Geophys. Res. Atmos.*, **118**, 5736–5749, doi:10.1002/jgrd.50419.
- Godfrey, J. S., R. A. Houze Jr., R. H. Johnson, R. Lukas, J.-L. Redelsperger, A. Sumi, and R. Weller, 1998: Coupled Ocean–Atmosphere Response Experiment (COARE): An interim report. *J. Geophys. Res.*, **103**, 14 395–14 450, doi:10.1029/97JC03120.
- Gottschalck, J., P. E. Roundy, C. J. Schreck III, A. Vintzileos, and C. Zhang, 2013: Large-scale atmospheric and oceanic conditions during the 2011–12 DYNAMO field campaign. *Mon. Wea. Rev.*, **141**, 4173–4196, doi:10.1175/MWR-D-13-00022.1.
- Halverson, J. B., B. S. Ferrier, T. M. Rickenbach, J. Simpson, and W.-K. Tao, 1999: An ensemble of convective systems on 11 February 1993 during TOGA COARE: Morphology, rainfall characteristics, and anvil cloud interactions. *Mon. Wea. Rev.*, **127**, 1208–1228, doi:10.1175/1520-0493(1999)127<1208:AEOSCO>2.0.CO;2.
- Houze, R. A., Jr., 2004: Mesoscale convective systems. *Rev. Geophys.*, **42**, RG4003, doi:10.1029/2004RG000150.
- Hu, Q., and D. A. Randall, 1994: Low-frequency oscillations in radiative–convective systems. *J. Atmos. Sci.*, **51**, 1089–1099, doi:10.1175/1520-0469(1994)051<1089:LFOIRC>2.0.CO;2.
- Huffman, G. J., and Coauthors, 2007: The TRMM Multisatellite Precipitation Analysis (TMPA): Quasi-global, multiyear, combined-sensor precipitation estimates at fine scales. *J. Hydrometeorol.*, **8**, 38–55, doi:10.1175/JHM560.1.
- Hung, M.-P., J.-L. Lin, W. Wang, D. Kim, T. Shinoda, and S. J. Weaver, 2013: MJO and convectively coupled equatorial waves simulated by CMIP5 climate models. *J. Climate*, **26**, 6185–6214, doi:10.1175/JCLI-D-12-00541.1.
- Johnson, R. H., and P. E. Ciesielski, 2013: Structure and properties of Madden–Julian oscillations deduced from DYNAMO sounding arrays. *J. Atmos. Sci.*, **70**, 3157–3179, doi:10.1175/JAS-D-13-065.1.
- , T. M. Rickenbach, S. A. Rutledge, P. E. Ciesielski, and W. H. Schubert, 1999: Trimodal characteristics of tropical convection. *J. Climate*, **12**, 2397–2418, doi:10.1175/1520-0442(1999)012<2397:TCOTC>2.0.CO;2.
- Kemball-Cook, S. R., and B. C. Weare, 2001: The onset of convection in the Madden–Julian oscillation. *J. Climate*, **14**, 780–793, doi:10.1175/1520-0442(2001)014<0780:TOOCIT>2.0.CO;2.
- Kikuchi, K., and Y. N. Takayabu, 2004: The development of organized convection associated with the MJO during TOGA COARE IOP: Trimodal characteristics. *Geophys. Res. Lett.*, **31**, L10101, doi:10.1029/2004GL019601.
- Kiladis, G. N., K. H. Straub, and P. T. Haertel, 2005: Zonal and vertical structure of the Madden–Julian oscillation. *J. Atmos. Sci.*, **62**, 2790–2809, doi:10.1175/JAS3520.1.
- Kim, D., and Coauthors, 2009: Application of MJO simulation diagnostics to climate models. *J. Climate*, **22**, 6413–6436, doi:10.1175/2009JCLI3063.1.
- Lau, K.-M., and P. H. Chan, 1985: Aspects of the 40–50 day oscillation during the northern winter as inferred from outgoing longwave radiation. *Mon. Wea. Rev.*, **113**, 1889–1909, doi:10.1175/1520-0493(1985)113<1889:AOTDOD>2.0.CO;2.
- , and —, 1986: Aspects of the 40–50 day oscillation during the northern summer as inferred from outgoing longwave radiation. *Mon. Wea. Rev.*, **114**, 1354–1367, doi:10.1175/1520-0493(1986)114<1354:AOTDOD>2.0.CO;2.
- , and H.-T. Wu, 2010: Characteristics of precipitation, cloud, and latent heating associated with the Madden–Julian oscillation. *J. Climate*, **23**, 504–518, doi:10.1175/2009JCLI2920.1.
- Lin, J.-L., and B. Mapes, 2004: Wind shear effects on cloud-radiation feedback in the western Pacific warm pool. *Geophys. Res. Lett.*, **31**, L16118, doi:10.1029/2004GL020199.
- , —, M. Zhang, and M. Newman, 2004: Stratiform precipitation, vertical heating profiles, and the Madden–Julian oscillation. *J. Atmos. Sci.*, **61**, 296–309, doi:10.1175/1520-0469(2004)061<0296:SPVHPA>2.0.CO;2.
- , and Coauthors, 2006: Tropical intraseasonal variability in 14 IPCC AR4 climate models. Part I: Convective signals. *J. Climate*, **19**, 2665–2690, doi:10.1175/JCLI3735.1.
- Lin, X., and R. H. Johnson, 1996: Kinematic and thermodynamic characteristics of the flow over the western Pacific warm pool during TOGA COARE. *J. Atmos. Sci.*, **53**, 695–715, doi:10.1175/1520-0469(1996)053<0695:KATCOT>2.0.CO;2.
- Liu, C., E. J. Zipser, D. J. Cecil, S. W. Nesbitt, and S. Sherwood, 2008: A cloud and precipitation feature database from nine years of TRMM observations. *J. Appl. Meteor. Climatol.*, **47**, 2712–2728, doi:10.1175/2008JAMC1890.1.
- Madden, R. A., and P. R. Julian, 1971: Detection of a 40–50 day oscillation in the zonal wind in the tropical Pacific. *J. Atmos. Sci.*, **28**, 702–708, doi:10.1175/1520-0469(1971)028<0702:DOADOI>2.0.CO;2.
- , and —, 1972: Description of global-scale circulation cells in the tropics with a 40–50 day period. *J. Atmos. Sci.*, **29**, 1109–1123, doi:10.1175/1520-0469(1972)029<1109:DOGSCC>2.0.CO;2.
- Maloney, E. D., 2009: The moist static energy budget of a composite tropical intraseasonal oscillation in a climate model. *J. Climate*, **22**, 711–729, doi:10.1175/2008JCLI2542.1.

- , and D. L. Hartmann, 1998: Frictional moisture convergence in a composite life cycle of the Madden–Julian Oscillation. *J. Climate*, **11**, 2387–2403, doi:[10.1175/1520-0442\(1998\)011<2387:FMCIAC>2.0.CO;2](https://doi.org/10.1175/1520-0442(1998)011<2387:FMCIAC>2.0.CO;2).
- Mapes, B. E., and R. A. Houze Jr., 1993: Cloud clusters and superclusters over the oceanic warm pool. *Mon. Wea. Rev.*, **121**, 1398–1416, doi:[10.1175/1520-0493\(1993\)121<1398:CCASOT>2.0.CO;2](https://doi.org/10.1175/1520-0493(1993)121<1398:CCASOT>2.0.CO;2).
- , S. Tulich, J. Lin, and P. Zuidema, 2006: The mesoscale convection life cycle: Building block or prototype for large-scale tropical waves? *Dyn. Atmos. Oceans*, **42**, 3–29, doi:[10.1016/j.dynatmoce.2006.03.003](https://doi.org/10.1016/j.dynatmoce.2006.03.003).
- McPhaden, M. J., and Coauthors, 2009: RAMA: The Research Moored Array for African–Asian–Australian Monsoon Analysis and Prediction. *Bull. Amer. Meteor. Soc.*, **90**, 459–480, doi:[10.1175/2008BAMS2608.1](https://doi.org/10.1175/2008BAMS2608.1).
- Morita, J., Y. N. Takayabu, S. Shige, and Y. Kodama, 2006: Analysis of rainfall characteristics of the Madden–Julian oscillation using TRMM satellite data. *Dyn. Atmos. Oceans*, **42**, 107–126, doi:[10.1016/j.dynatmoce.2006.02.002](https://doi.org/10.1016/j.dynatmoce.2006.02.002).
- Moum, J. N., and Coauthors, 2014: Air–sea interactions from westerly wind burst events during the November 2011 MJO in the Indian Ocean. *Bull. Amer. Meteor. Soc.*, doi:[10.1175/BAMS-D-12-00225.1](https://doi.org/10.1175/BAMS-D-12-00225.1), in press.
- Nakazawa, T., 1988: Tropical super clusters within intraseasonal variations over the western Pacific. *J. Meteor. Soc. Japan*, **66**, 823–839.
- Oye, D., and M. Case, 1995: REORDER: A program for gridding radar data: Installation and use manual for the UNIX version. NCAR Atmospheric Technology Division, 30 pp. [Available from NCAR, P.O. Box 3000, Boulder, CO 80307.]
- Petersen, W. A., S. A. Rutledge, and R. E. Orville, 1996: Cloud-to-ground lightning observations from TOGA COARE: Selected results and lightning location algorithms. *Mon. Wea. Rev.*, **124**, 602–620, doi:[10.1175/1520-0493\(1996\)124<0602:CTGLOF>2.0.CO;2](https://doi.org/10.1175/1520-0493(1996)124<0602:CTGLOF>2.0.CO;2).
- Pohjola, H., and A. Mäkelä, 2013: The comparison of GLD360 and EUCLID lightning location systems in Europe. *Atmos. Res.*, **123**, 117–128, doi:[10.1016/j.atmosres.2012.10.019](https://doi.org/10.1016/j.atmosres.2012.10.019).
- Powell, S., and R. A. Houze Jr., 2013: The cloud population and onset of the Madden–Julian oscillation over the Indian Ocean during DYNAMO-AMIE. *J. Geophys. Res. Atmos.*, **118**, 11 979–11 995, doi:[10.1002/2013JD020421](https://doi.org/10.1002/2013JD020421).
- Randall, D., M. Khairoutdinov, A. Arakawa, and W. Grabowski, 2003: Breaking the cloud parameterization deadlock. *Bull. Amer. Meteor. Soc.*, **84**, 1547–1564, doi:[10.1175/BAMS-84-11-1547](https://doi.org/10.1175/BAMS-84-11-1547).
- Rickenbach, T. M., and S. A. Rutledge, 1998: Convection in TOGA COARE: Horizontal scale, morphology, and rainfall production. *J. Atmos. Sci.*, **55**, 2715–2729, doi:[10.1175/1520-0469\(1998\)055<2715:CITCHS>2.0.CO;2](https://doi.org/10.1175/1520-0469(1998)055<2715:CITCHS>2.0.CO;2).
- Riley, E. M., B. E. Mapes, and S. N. Tulich, 2011: Clouds associated with the Madden–Julian oscillation: A new perspective from CloudSat. *J. Atmos. Sci.*, **68**, 3032–3051, doi:[10.1175/JAS-D-11-030.1](https://doi.org/10.1175/JAS-D-11-030.1).
- Rui, H., and B. Wang, 1990: Development characteristics and dynamic structure of tropical intraseasonal convection anomalies. *J. Atmos. Sci.*, **47**, 357–379, doi:[10.1175/1520-0469\(1990\)047<0357:DCADSO>2.0.CO;2](https://doi.org/10.1175/1520-0469(1990)047<0357:DCADSO>2.0.CO;2).
- Rutledge, S. A., E. R. Williams, and T. D. Keenan, 1992: The Down Under Doppler and Electricity Experiment (DUNDEE): Overview and preliminary results. *Bull. Amer. Meteor. Soc.*, **73**, 3–16, doi:[10.1175/1520-0477\(1992\)073<0003:TDUDAE>2.0.CO;2](https://doi.org/10.1175/1520-0477(1992)073<0003:TDUDAE>2.0.CO;2).
- Said, R. K., U. S. Inan, and K. L. Cummins, 2010: Long-range lightning geolocation using a VLF radio atmospheric waveform bank. *J. Geophys. Res.*, **115**, D23108, doi:[10.1029/2010JD013863](https://doi.org/10.1029/2010JD013863).
- , M. B. Cohen, and U. S. Inan, 2013: Highly intense lightning over the oceans: Estimated peak currents from global GLD360 observations. *J. Geophys. Res. Atmos.*, **118**, 6905–6915, doi:[10.1002/jgrd.50508](https://doi.org/10.1002/jgrd.50508).
- Salby, M. L., and H. H. Hendon, 1994: Intraseasonal behavior of clouds, temperature, and motion in the tropics. *J. Atmos. Sci.*, **51**, 2207–2224, doi:[10.1175/1520-0469\(1994\)051<2207:IBOCTA>2.0.CO;2](https://doi.org/10.1175/1520-0469(1994)051<2207:IBOCTA>2.0.CO;2).
- Saxen, T. R., and S. A. Rutledge, 2000: Surface rainfall–cold cloud fractional coverage relationship in TOGA COARE: A function of vertical wind shear. *Mon. Wea. Rev.*, **128**, 407–415, doi:[10.1175/1520-0493\(2000\)128<0407:SRCCFC>2.0.CO;2](https://doi.org/10.1175/1520-0493(2000)128<0407:SRCCFC>2.0.CO;2).
- Shie, C.-L., W.-K. Tao, J. Simpson, and C.-H. Sui, 2003: Quasi-equilibrium states in the Tropics simulated by a cloud-resolving model. Part I: Specific features and budget analysis. *J. Climate*, **16**, 817–833, doi:[10.1175/1520-0442\(2003\)016<0817:QESITT>2.0.CO;2](https://doi.org/10.1175/1520-0442(2003)016<0817:QESITT>2.0.CO;2).
- Short, D. A., P. A. Kucera, B. S. Ferrier, J. C. Gerlach, S. A. Rutledge, and O. W. Thiele, 1997: Shipboard radar rainfall patterns within the TOGA COARE IFA. *Bull. Amer. Meteor. Soc.*, **78**, 2817–2836, doi:[10.1175/1520-0477\(1997\)078<2817:SRPWT>2.0.CO;2](https://doi.org/10.1175/1520-0477(1997)078<2817:SRPWT>2.0.CO;2).
- Steiner, M., R. A. Houze Jr., and S. E. Yuter, 1995: Climatological characterization of three-dimensional storm structure from operational radar and rain gauge data. *J. Appl. Meteor.*, **34**, 1978–2007, doi:[10.1175/1520-0450\(1995\)034<1978:CCOTDS>2.0.CO;2](https://doi.org/10.1175/1520-0450(1995)034<1978:CCOTDS>2.0.CO;2).
- Stephens, G. L., P. J. Webster, R. H. Johnson, R. Engelen, and T. S. L’Ecuyer, 2004: Observational evidence for the mutual regulation of the tropical hydrological cycle and tropical sea surface temperatures. *J. Climate*, **17**, 2213–2224, doi:[10.1175/1520-0442\(2004\)017<2213:OEFTMR>2.0.CO;2](https://doi.org/10.1175/1520-0442(2004)017<2213:OEFTMR>2.0.CO;2).
- Sui, C.-H., and K. M. Lau, 1992: Multiscale phenomena in the tropical atmosphere over the western Pacific. *Mon. Wea. Rev.*, **120**, 407–430, doi:[10.1175/1520-0493\(1992\)120<0407:MPITTA>2.0.CO;2](https://doi.org/10.1175/1520-0493(1992)120<0407:MPITTA>2.0.CO;2).
- Tao, W.-K., J. Simpson, C.-H. Sui, B. Ferrier, S. Lang, J. Scala, M. D. Chou, and K. Pickering, 1993: Heating, moisture, and water budgets of tropical and midlatitude squall lines: Comparisons and sensitivity to longwave radiation. *J. Atmos. Sci.*, **50**, 673–690, doi:[10.1175/1520-0469\(1993\)050<0673:HMAWBO>2.0.CO;2](https://doi.org/10.1175/1520-0469(1993)050<0673:HMAWBO>2.0.CO;2).
- , J.-P. Chen, Z. Li, C. Wang, and C. Zhang, 2012: Impact of aerosols on convective clouds and precipitation. *Rev. Geophys.*, **50**, RG2001, doi:[10.1029/2011RG000369](https://doi.org/10.1029/2011RG000369).
- Thompson, E., S. Rutledge, B. Dolan, R. Rilling, M. Dixon, S. Ellis, and W. Xu, 2013: Radar rainfall estimation during DYNAMO. *36th Conf. on Radar Meteorology*, Breckenridge, CO, Amer. Meteor. Soc., 229. [Available online at <https://ams.confex.com/ams/36Radar/webprogram/Paper228452.html>.]
- Tian, B., D. E. Waliser, E. J. Fetzer, B. H. Lambrigtsen, Y. L. Yung, and B. Wang, 2006: Vertical moist thermodynamic structure and spatial–temporal evolution of the MJO in AIRS observations. *J. Atmos. Sci.*, **63**, 2462–2485, doi:[10.1175/JAS3782.1](https://doi.org/10.1175/JAS3782.1).
- Tromeur, E., and W. B. Rossow, 2010: Interaction of tropical deep convection with the large-scale circulation in the MJO. *J. Climate*, **23**, 1837–1853, doi:[10.1175/2009JCLI3240.1](https://doi.org/10.1175/2009JCLI3240.1).
- Virts, K. S., J. M. Wallace, Q. Fu, and T. P. Ackerman, 2010: Tropical tropopause transition layer cirrus as represented by CALIPSO lidar observations. *J. Atmos. Sci.*, **67**, 3113–3129, doi:[10.1175/2010JAS3412.1](https://doi.org/10.1175/2010JAS3412.1).

- Vitart, F., and F. Molteni, 2010: Simulation of the Madden–Julian oscillation and its teleconnections in the ECMWF forecast system. *Quart. J. Roy. Meteor. Soc.*, **136**, 842–855, doi:[10.1002/qj.623](https://doi.org/10.1002/qj.623).
- Weickmann, K. M., G. R. Lussky, and J. E. Kutzbach, 1985: Intraseasonal (30–60 day) fluctuations of outgoing longwave radiation and 250 mb streamfunction during northern winter. *Mon. Wea. Rev.*, **113**, 941–961, doi:[10.1175/1520-0493\(1985\)113<0941:IDFOOL>2.0.CO;2](https://doi.org/10.1175/1520-0493(1985)113<0941:IDFOOL>2.0.CO;2).
- Wheeler, M., and H. H. Hendon, 2004: An all-season real-time multivariate MJO index: Development of an index for monitoring and prediction. *Mon. Wea. Rev.*, **132**, 1917–1932, doi:[10.1175/1520-0493\(2004\)132<1917:AARMMI>2.0.CO;2](https://doi.org/10.1175/1520-0493(2004)132<1917:AARMMI>2.0.CO;2).
- Williams, E. R., 1989: The tripole structure of thunderstorms. *J. Geophys. Res.*, **94**, 13 151–13 167, doi:[10.1029/JD094iD11p13151](https://doi.org/10.1029/JD094iD11p13151).
- , and S. Stanfill, 2002: The physical origin of the land–ocean contrast in lightning activity. *C. R. Phys.*, **3**, 1277–1292, doi:[10.1016/S1631-0705\(02\)01407-X](https://doi.org/10.1016/S1631-0705(02)01407-X).
- , S. A. Rutledge, S. G. Geotis, N. Renno, E. Rasmussen, and T. Rickenbach, 1992: A radar and electrical study of tropical “hot towers.” *J. Atmos. Sci.*, **49**, 1386–1395, doi:[10.1175/1520-0469\(1992\)049<1386:ARAESO>2.0.CO;2](https://doi.org/10.1175/1520-0469(1992)049<1386:ARAESO>2.0.CO;2).
- Yanai, M., B. Chen, and W.-W. Tung, 2000: The Madden–Julian oscillation observed during the TOGA COARE IOP: Global view. *J. Atmos. Sci.*, **57**, 2374–2396, doi:[10.1175/1520-0469\(2000\)057<2374:TMJOOD>2.0.CO;2](https://doi.org/10.1175/1520-0469(2000)057<2374:TMJOOD>2.0.CO;2).
- Yoneyama, K., and Coauthors, 2008: MISO field experiment in the equatorial Indian Ocean. *Bull. Amer. Meteor. Soc.*, **89**, 1889–1903, doi:[10.1175/2008BAMS2519.1](https://doi.org/10.1175/2008BAMS2519.1).
- , C. Zhang, and C. N. Long, 2013: Tracking pulses of the Madden–Julian oscillation. *Bull. Amer. Meteor. Soc.*, **94**, 1871–1891, doi:[10.1175/BAMS-D-12-00157.1](https://doi.org/10.1175/BAMS-D-12-00157.1).
- Yuan, J., and R. A. Houze Jr., 2013: Deep convective systems observed by A-Train in the tropical Indo-Pacific region affected by the MJO. *J. Atmos. Sci.*, **70**, 465–486, doi:[10.1175/JAS-D-12-057.1](https://doi.org/10.1175/JAS-D-12-057.1).
- Yuan, T., L. A. Remer, K. E. Pickering, and H. Yu, 2011: Observational evidence of aerosol enhancement of lightning activity and convective invigoration. *Geophys. Res. Lett.*, **38**, L04701, doi:[10.1029/2010GL046052](https://doi.org/10.1029/2010GL046052).
- Zhang, C., 2005: Madden–Julian oscillation. *Rev. Geophys.*, **43**, RG2003, doi:[10.1029/2004RG000158](https://doi.org/10.1029/2004RG000158).
- , 2013: Madden–Julian oscillation: Bridging weather and climate. *Bull. Amer. Meteor. Soc.*, **94**, 1849–1870, doi:[10.1175/Bams-D-12-00026.1](https://doi.org/10.1175/Bams-D-12-00026.1).
- , M. Dong, S. Gualdi, H. H. Hendon, E. D. Maloney, A. Marshall, K. R. Sperber, and W. Wang, 2006: Simulations of the Madden–Julian oscillation in four pairs of coupled and uncoupled global models. *Climate Dyn.*, **27**, 573–592, doi:[10.1007/s00382-006-0148-2](https://doi.org/10.1007/s00382-006-0148-2).
- Zhang, G. J., and X. Song, 2009: Interaction of deep and shallow convection is key to Madden–Julian oscillation simulation. *Geophys. Res. Lett.*, **36**, L09708, doi:[10.1029/2009GL037340](https://doi.org/10.1029/2009GL037340).
- Zipser, E. J., 1994: Deep cumulonimbus cloud systems in the tropics with and without lightning. *Mon. Wea. Rev.*, **122**, 1837–1851, doi:[10.1175/1520-0493\(1994\)122<1837:DCCSIT>2.0.CO;2](https://doi.org/10.1175/1520-0493(1994)122<1837:DCCSIT>2.0.CO;2).
- Zuluaga, M. D., and R. A. Houze Jr., 2013: Evolution of the population of precipitating convective systems over the equatorial Indian Ocean in active phases of the Madden–Julian oscillation. *J. Atmos. Sci.*, **70**, 2713–2725, doi:[10.1175/JAS-D-12-0311.1](https://doi.org/10.1175/JAS-D-12-0311.1).